minerals

MDPI

Article

Lattice-Preferred Orientation and Seismic Anisotropy of Minerals in Retrograded Eclogites from Xitieshan, Northwestern China, and Implications for Seismic Reflectance of Rocks in the Subduction Zone

Jaeseok Lee and Haemyeong Jung *

Tectonophysics Laboratory, School of Earth and Environmental Sciences, Seoul National University, Seoul 08826, Korea; shoo3680@snu.ac.kr

* Correspondence: hjung@snu.ac.kr; Tel.: +82-2-880-6733

Abstract: Various rock phases, including those in subducting slabs, impact seismic anisotropy in subduction zones. The seismic velocity and anisotropy of rocks are strongly affected by the lattice-preferred orientation (LPO) of minerals; this was measured in retrograded eclogites from Xitieshan, northwest China, to understand the seismic velocity, anisotropy, and seismic reflectance of the upper part of the subducting slab. For omphacite, an S-type LPO was observed in three samples. For amphibole, the <001> axes were aligned subparallel to the lineation, and the (010) poles were aligned subnormal to foliation. The LPOs of amphibole and omphacite were similar in most samples. The misorientation angle between amphibole and neighboring omphacite was small, and a lack of intracrystalline deformation features was observed in the amphibole. This indicates that the LPO of amphibole was formed by the topotactic growth of amphibole during retrogression of eclogites. The P-wave anisotropy of amphibole in retrograded eclogites was large (approximately 3.7–7.3%). The seismic properties of retrograded eclogites and amphibole were similar, indicating that the seismic properties of retrograded eclogites are strongly affected by the amphibole LPO. The contact boundary between serpentinized peridotites and retrograded eclogites showed a high reflection coefficient, indicating that a reflected seismic wave can be easily detected at this boundary.

Keywords: retrograded eclogite; amphibole; topotactic growth; reflection coefficient; omphacite; subduction zone; lattice-preferred orientation; Xitieshan eclogite; seismic anisotropy

Citation: Lee, J.; Jung, H. Lattice-Preferred Orientation and Seismic Anisotropy of Minerals in Retrograded Eclogites from Xitieshan, Northwestern China, and Implications for Seismic Reflectance of Rocks in the Subduction Zone. *Minerals* **2021**, *11*, 380. https://doi.org/10.3390/min11040380

Academic Editor: Tatsuki Tsujimori

Received: 17 February 2021
Accepted: 31 March 2021
Published: 2 April 2021

1. Introduction

Subduction zones are known to have varying seismic velocity structures and anisotropies caused by subducting slabs [1–4]. Seismic velocity and anisotropy are strongly affected by the lattice-preferred orientation (LPO) of elastically anisotropic minerals [5–24]. When a slab is subducted under high-pressure and high-temperature conditions, the major rock phase of the upper subducting slab transforms into eclogite, which consists mainly of omphacite and garnet [8,25–28]. Garnet has a relatively high seismic velocity, and omphacite has a strong seismic anisotropy [5,6,23,29]. Eclogites that are formed at the deep part of the subducting slab are known to have a faster seismic velocity—similar to that of the upper mantle (V_P ~ 8.0 km/s)—than the surrounding rocks, and they have a strong seismic anisotropy, thus affecting various seismic velocities and anisotropies in subduction zones [30,31].

In addition, when eclogite appears near the surface due to slab break-off in the subduction zone, the eclogite is retrograded to form amphibole under low-pressure and low-temperature conditions [22,32]. Amphibole exists in subducting slabs under lower-pressure and lower-temperature conditions than eclogite stability conditions, and in the middle to lower crust [33], whereas the LPO development of amphibole is known to produce a strong seismic anisotropy [18,34–36]. Therefore, deformed retrograded eclogites may represent

seismic velocity and anisotropy in relatively shallow subducting slabs [5,6,20,31,37–49]. Measuring the LPOs of omphacite, amphibole, and garnet in retrograded eclogites can therefore be useful in understanding the seismic velocity and anisotropy of subducting slabs in subduction zones.

In addition, owing to the various seismic velocity structures of subduction zones, seismic waves tend to be reflected at the boundary of rock phases with varying seismic velocities. In particular, the upper parts of subducting slabs have a fast seismic velocity [6], which can cause a difference in seismic velocity from surrounding rocks and may reflect seismic waves due to this difference in seismic velocity [6,50–53]. In previous studies, the reflection coefficient (R_C) was suggested to quantify the degree of seismic wave reflection [6,50,51]. Calculating the R_C of the boundaries between retrograded eclogites and surrounding rocks, using their P-wave velocities, and comparing the degree of retrogression of eclogites and R_C of these boundaries may explain the degree of reflection of seismic waves at these boundaries.

Garnet is a seismically nearly isotropic mineral with a cubic shape that develops little LPO [54]. The LPOs of other minerals in retrograded eclogites—amphibole and omphacite—have been studied in both naturally and experimentally deformed rocks. Four types of LPOs of amphibole have been reported: type I, type II, type III, and type IV [18,36]. A previous experimental study on amphibolite, which was conducted at a pressure of 1 GPa and temperatures of 480–700 °C [18], reported that the type I amphibole LPO was formed under relatively low-stress and low-temperature conditions and is characterized as the <100> axes aligned subnormal to foliation and <001> axes aligned subparallel to lineation. The type II amphibole LPO was formed under relatively high-stress and moderate-temperature deformation conditions and is characterized as <100> axes aligned subnormal to foliation and (010) poles aligned subparallel to lineation. The type III amphibole LPO was formed under relatively low-stress and high-temperature deformation conditions and is characterized as <100> axes aligned subnormal to foliation, with both <001> axes and (010) poles forming a girdle shape subparallel to foliation [18]. A recent experimental study reported that the type IV amphibole LPO can be formed owing to high strain [36] and is characterized as <001> axes aligned subparallel to lineation, with both <100> axes and (110) poles forming a girdle shape subnormal to the shear direction [36]. Previously, the LPOs of amphibole, similar to the type IV amphibole LPO, have been reported in naturally deformed rocks, which were observed in metabasites from southwestern Spain and northwest Scotland, retrogressed Limo harzburgites from northwestern Spain, and amphibolites from Spain [44,55–58]. On the other hand, an amphibole LPO has also been reported in which the (010) poles are aligned subnormal to foliation and the <001> axes are aligned subparallel to lineation [44,59,60].

Three types of omphacite LPOs have been reported: L-, S-, and LS-type omphacite LPOs [61]. The S-type omphacite LPO is characterized as the <001> axis of omphacite forming a girdle parallel to foliation and the (010) pole of omphacite aligned subnormal to foliation. The L-type omphacite LPO is characterized as the <001> axis of omphacite aligned subparallel to lineation and the (010) pole of omphacite forming a girdle subnormal to lineation. The LS-type omphacite LPO is characterized as the <001> axis of omphacite aligned subparallel to lineation and the (010) pole of omphacite aligned subnormal to foliation, indicating a (010) <001> slip system [20,61].

The seismic reflection coefficient (R_C) was previously calculated only for the boundary between fresh eclogite and neighboring rocks [6,50]. In this study, the omphacite and amphibole LPOs in the retrograded eclogites from Xitieshan, northwest China, which represent various degrees of retrogression (35–90%), were measured. The Xitieshan eclogites are useful for studying the relationship between the degree of retrogression and seismic velocity, anisotropy, and reflectance. The seismic velocity and anisotropy of retrograded eclogites were calculated using the LPOs of minerals, and the effect of the amphibole LPO on the seismic velocity and anisotropy of retrograded eclogites was also investigated. R_C was calculated using the P-wave velocity, and R_C was examined to understand the seismic

wave reflectance of the boundaries between the retrograded eclogites and neighboring rocks. The results of the present study provide a valuable opportunity to understand the seismic velocity, anisotropy, and reflectance of retrograded eclogites and to identify the boundary between the subducting slab and mantle wedge in various subduction zones.

2. Geological Settings

Xitieshan is located in the central part of the North Qaidam ultra-high-pressure (UHP) metamorphic belt, which is located at the northeastern margin of the Tibetan Plateau in northwestern China (Figures 1 and 2). The North Qaidam UHP metamorphic belt is a typical Alpine-type continental collision/subduction zone, containing the characteristic continental rock association of granitic and pelitic gneiss with intercalated eclogite and peridotite [33,34,62–64]. From the southeastern part, four individual UHP terranes were observed: the Dulan eclogite-bearing terrane, the Xitieshan eclogite-bearing terrane, the Lulingshan garnet peridotite-bearing terrane, and the Yuka eclogite-bearing terrane. Coesite and diamonds were found as inclusions in zircon and garnet in all four terranes, proving that these four terranes had been under UHP metamorphic conditions, similar to other continental UHP metamorphic terranes in China [64].

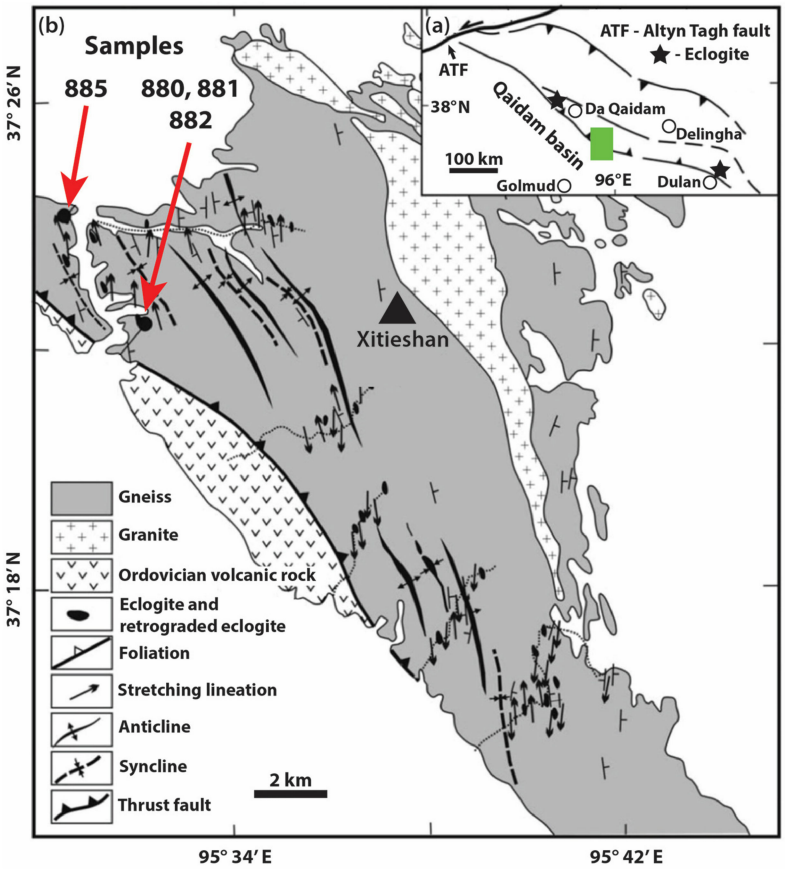

Figure 1. (**a**) Schematic geological map showing the North Qaidam ultra-high-pressure (UHP) metamorphic belt, northwestern China. (**b**) Study area and geological map of Xitieshan area. Green rectangle area in (**a**) was magnified (modified after Zhang et al. [65]).

Figure 2. Photographs of the Xitieshan outcrop. (**a**) Large view of the Xitieshan Mountain containing retrograded eclogites and (**b**) magnified view of the rectangle in (**a**) showing a body of retrograded eclogite.

The eclogites in the Xitieshan terrane can be divided into two groups: bimineralic eclogite and phengite-bearing eclogite. Bimineralic eclogite is the major component of the Xitishan terrane, whereas phengite-bearing eclogite concentrations are minor and can only be seen in the Huangyanggou area. Most eclogites in the Xitishan terrane were retrograded into garnet amphibolite or amphibolite. The original eclogite can be found in the center of the large bodies.

The Xitieshan eclogites experienced two stages of retrogression. According to previous studies [66,67], the peak pressure and temperature conditions of metamorphism of the Xitieshan eclogite were P = 2.71–3.17 GPa and T = 751–791 °C. In the first stage (isothermal decompression), the proportion of omphacite and garnet in the sample decreased, while the proportion of amphibole and plagioclase increased at a temperature of T ~ 750 °C when pressure decreased from P ~ 2.3 GPa to P ~ 1.5 GPa. In the second stage (symplectite formation), symplectite of diopside, plagioclase, and edenite appeared under the condition of P = 8–12 kbar and T = 660–720 °C [67].

In addition to the Xitieshan area, geochronology data reported that there were two major different ages measured using zircon: 750–800 Ma and 877 ± 8 Ma were calculated in the cores of the zircon, and 440–460 Ma and 433 ± 3 Ma were calculated at the rim of the zircon. Based on the ages calculated in the core of the zircon, some of the Xitieshan terrane eclogites were produced in Neoproterozoic protoliths much before the Paleozoic subduction or collision event occurred in the North Qaidam UHP metamorphism. Eclogite metamorphism occurred in the age calculated at the rim of zircon [67–71].

3. Methods

3.1. Measurement of Lattice-Preferred Orientation (LPO) of Minerals

Foliation of a rock was defined by compositional layering of amphibole and garnet, and lineation was determined by the shape-preferred orientation of minerals on foliation, using the projection function method [72]. Thin sections were made in the XZ plane to measure the LPO, the X axis was set parallel to lineation, and the Z axis was set normal to foliation.

The LPOs of the samples were measured using electron back-scattered diffraction (EBSD) using a JEOL-JSM-7100 field emission scanning electron microscope (FE-SEM) with AZTEC and HKL Channel 5 software (5.12.74.0) installed at the School of Earth and Environmental Sciences (SEES), Seoul National University (SNU). Detailed settings of the EBSD mapping are provided in Table 1. An accelerating voltage of 20 kV and a working distance of 20 mm with a tilting angle of 70° were the main settings of the FE-SEM with EBSD. The samples were observed using automatic mapping mode, with a step size of 23 to 35 μm, depending on the grain size of most of the samples. To eliminate the oversampling of large grains, pole figures were constructed from one point per grain [73]. The omphacite LPOs, which were in direct contact with amphibole single crystals, were measured using a smaller step size (1 μm). The misorientation index (M-index) [74] was calculated to estimate the fabric strength of the sample using the uncorrelated grain pairs obtained from the orientation data. The M-index ranged from 0 (random) to 1 (single grain). The misorientation angle was measured using HKL Channel 5 software (Tango).

Table 1. Modal composition, aspect ratio, settings of electron back-scattered diffraction (EBSD) mapping, and estimated equilibrium temperature of samples.

Sample	Modal Composition (%)						Aspect Ratio of Minerals			EBSD Mapping		Temperature [a] (°C)
	Amp	Omp	Plag	Grt	Qtz	Others	XY	XZ	YZ	Step Size (μm)	Hit Rate (%)	
885	33.0	14.0	8.8	33.3	10.1	Mi 1.0	1.129	1.317	1.199	25	91.2	727 ± 40
881	51.9	19.6	10.7	16.2	1.4	Il 0.2	1.222	1.424	1.154	25	95.4	746 ± 50
880	53.4	13.2	25.2	2.0	5.6	Il 0.7	1.273	1.340	1.176	35	96.1	759 ± 50
882 *	91.5	1.3 *	3.3	3.6	0.1	Il 0.2	1.138	1.489	1.403	23	84.4	780 ± 30

Amp: amphibole; Omp: omphacite; Plag: plagioclase; Grt: garnet; Qtz: quartz; Mi: mica; Il: ilmenite. EBSD: electron back-scattered diffraction. [a] Equilibrium temperature using geothermometry (Ravna and Terry [75]; Ravna [76]). * Sample 882 is the most retrograded eclogite, and the composition of omphacite was changed to diopside. X: lineation, Z: normal to foliation, and Y: normal to X and Z.

3.2. Calculation of Seismic Velocity and Anisotropy

Seismic velocity and anisotropy were calculated using the orientation data of the minerals and the single-crystal elastic constants of amphibole [77] and omphacite [29] in sample 885, 880, and 881; diopside [78] in sample 882; garnet [54]; and plagioclase [79] using the Fortran program [80]. The whole-rock seismic velocity and anisotropy were calculated by combining the calculated results of individual minerals, including amphibole, garnet, and omphacite in samples 885, 880, and 881; diopside in sample 882; and all minor minerals, quartz [81], ilmenite [82], and mica [83], with weighted values for the number of grains.

AV_P indicates the anisotropy of the P-wave velocity in all propagation directions, calculated using Equation (1). AV_S indicates the anisotropy of split fast and slow S-wave velocity in the same propagation direction, calculated using Equation (2) [80].

$$AV_P = (V_{Pmax} - V_{Pmin})/[(V_{Pmax} + V_{Pmin})/2], \quad (1)$$

$$AV_S = (V_{Sfast} - V_{Sslow})/[(V_{Sfast} + V_{Sslow})/2] \quad (2)$$

3.3. Calculation of Reflection Coefficient

The reflection coefficient (R_C) was calculated for a seismic wave propagating perpendicular to the boundary between two rock types or layers. This concept is simple and allows the calculation of R_C as follows:

$$R_C = [V_P(//Z)_{1\rho1} - V_P(//Z)_{2\rho2}]/[V_P(//Z)_{1\rho1} + V_P(//Z)_{2\rho2}], \quad (3)$$

where $V_P(//Z)_{1\rho1}$ and $V_P(//Z)_{2\rho2}$ indicate the P-wave velocity propagating normal to the foliation in rocks/layers 1 and 2, respectively [6,50,51].

Reflection coefficients were calculated assuming a boundary between the studied samples and rocks expected to be stable near existing eclogite zones, such as amphibole peridotite [84], chlorite peridotite [85], lawsonite blueschist [8,86], epidote blueschist [87], garnet peridotite [87–89], peridotite complexes (lherzolite, harzburgite, dunite) [90–92], lawsonite eclogite [17], olivine complexes [93], spinel peridotite [94], serpentinite [95,96], serpentinized peridotite [92,97], felsic and mafic blueschist [98], dunite [99], and glaucophane schist (containing epidote or phengite) [100].

3.4. Micro-Raman Spectroscopy

A micro-Raman spectrometer located at the Tectonophysics Laboratory in SEES, SNU, was used to identify minerals clearly. This spectrometer was equipped with a 532 nm laser (10 mW power) and an optical microscope with a 50× objective lens. It had a resolution of 0.01 cm^{-1} over the wavenumber range of 50 to 3550 cm^{-1}, with a beam size of 0.67 μm. The spectrum was overlapped 32 times to reduce noise.

3.5. Analysis of Chemical Composition and Temperature Estimation

The chemical composition of the minerals in the samples was measured using a JEOL JXA-8530F Plus electron hyper probe installed at the Center for Research facility at Gyeongsang National University and at the National Center for Inter-University Research Facilities at Seoul National University, South Korea, using an acceleration voltage of 15 kV, a beam current of 10 nA, and a beam size of 5 μm in diameter. The amphibole phase was classified using the Excel spreadsheet provided by Locock [101] based on the classification of Hawthorne et al. [102].

The equilibrium temperature of the samples was estimated by thermometry of garnet–clinopyroxene Fe–Mg exchange [75,76], and the measured oxide mass percentages of garnet, clinopyroxene, amphibole, and minor minerals were used to calculate the equilibrium temperature.

4. Results

4.1. Sample Description and Microstructures

All samples were identified as retrograded eclogites, and the degree of retrogression of the samples varied depending on the sample. The samples had a high proportion of amphibole and plagioclase, and half of the clinopyroxene grains exhibited a symplectite structure of omphacite, diopside, and plagioclase, indicating that our samples were retrograded. The modal composition of rocks and the aspect ratio of minerals are shown in Table 1, and photomicrographs of the samples are shown in Figure 3. Sample 885 was a relatively fresh eclogite, whereas sample 882 was the most retrograded eclogite. Samples 881 and 880 showed an intermediate degree of retrogression, between that of samples 885 and 882. The phase of the minerals in sample 885 (the relatively fresh eclogite) was identified using micro-Raman spectroscopy. Clinopyroxene was identified as omphacite, with Raman peaks at 142, 338, 674, and 1016 cm^{-1}, whereas garnet in the same sample showed Raman peaks at 356 and 911 cm^{-1}. An unknown mineral found in the relatively fresh eclogite showing Raman peaks at 175, 300, and 1099 cm^{-1} was identified as zircon (Figure 4).

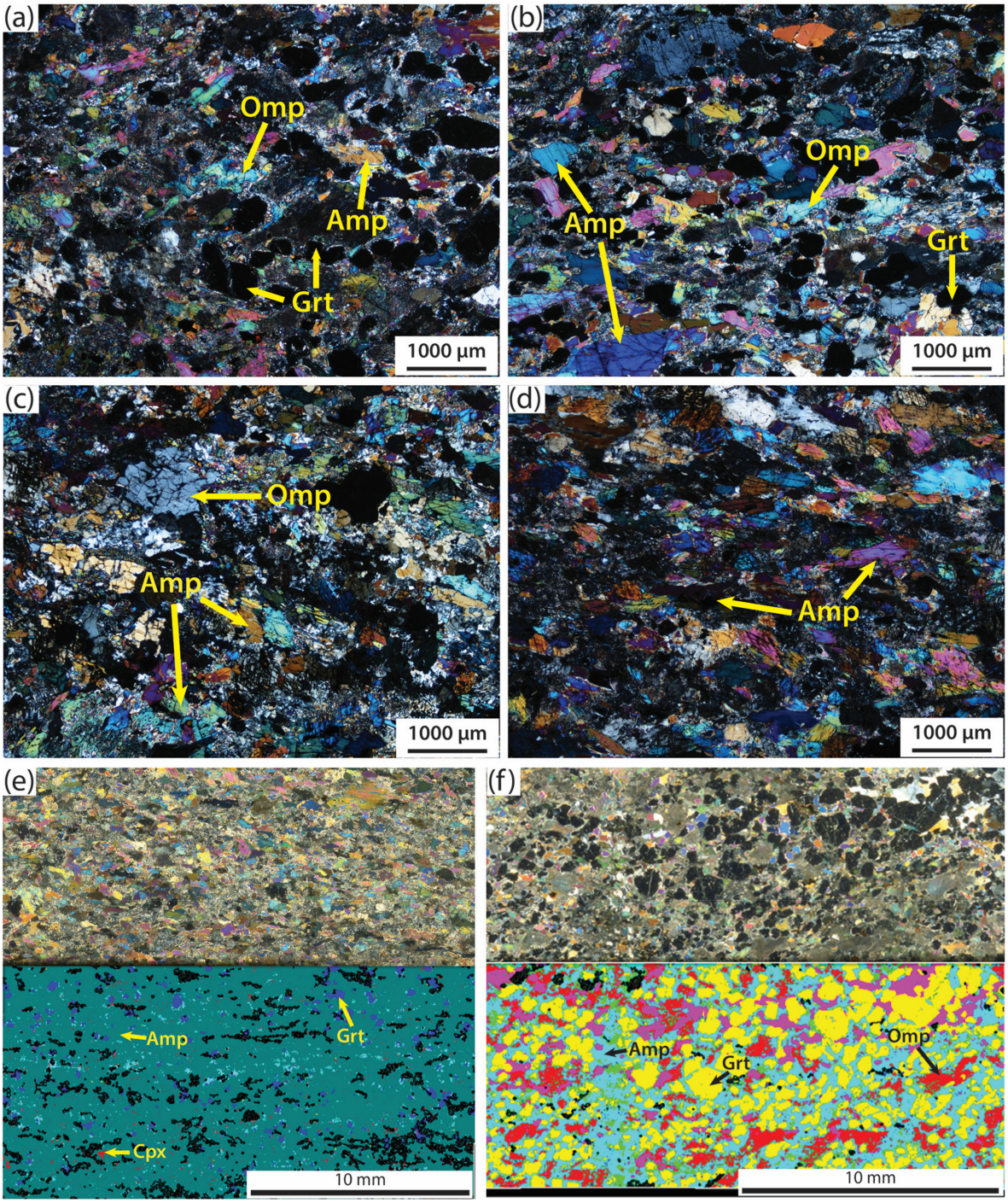

Figure 3. Photomicrograph of a thin section in the XZ plane of samples. (**a**) Sample 885, showing relatively fresh eclogite; (**b**) sample 881, showing retrograded eclogite illustrating a lack of intracrystalline deformation in amphibole; (**c**) sample 880, showing retrograded eclogite; (**d**) sample 882, the most severely retrograded eclogite showing elongated amphiboles and a well-developed foliation; (**e**) thin-section image of sample 882 in cross-polarized light (top) and EBSD phase map (bottom) (color codes: greenish blue, amphibole; blue, garnet; light blue, plagioclase; red, clinopyroxene; black, non-indexed points); and (**f**) thin-section image of sample 885 in cross-polarized light (top) and EBSD phase map (bottom) (color codes: light blue, amphibole; yellow, garnet; red, omphacite; purple, quartz; green, plagioclase; black, non-indexed points). Omp: omphacite; Amp: amphibole; Grt: garnet; Cpx: clinopyroxene.

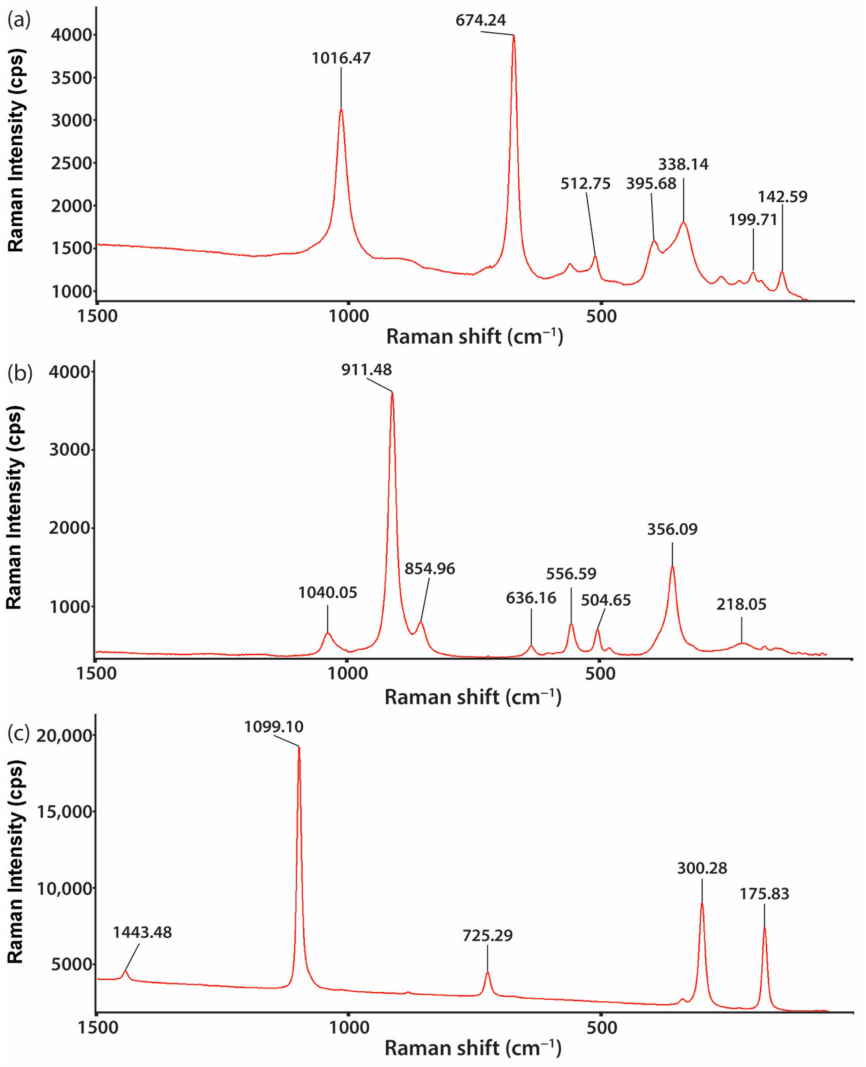

Figure 4. Micro-Raman spectra of (**a**) omphacite, (**b**) garnet, and (**c**) zircon in sample 885.

Amphibole and omphacite in the samples showed well-developed foliation (Figure 3b–f), but garnet showed less elongated grains than other minerals, indicating that garnet grains are less affected by deformation (Figure 3a,b,f). All mineral grains, except garnet, showed curved or angular-shaped grain boundaries, whereas garnet grains showed straight grain boundaries. Most of the amphibole grains showed cleavage in grains, with elongated grain shapes (Figure 3b,d). However, amphibole grains showed a lack of intracrystalline deformation features, such as undulose extinction or subgrains (Figure 3b,d).

4.2. Chemical Composition and Equilibrium Temperature

The chemical compositions of the minerals in the samples are listed in Table 2. Muscovite was found in two samples, 882 and 885, whereas the other samples, 880 and 881, did not contain muscovite. By analyzing the amphibole phase by chemical composition, amphibole in all the samples was found to be magnesiohornblende.

Table 2. Representative chemical composition (oxide mass, %) of minerals in samples.

Element	Sample 885								Sample 880				
	Amp	**Omp**	**Grt**	**Mus**	**Ru**	**Ilme**	**Plg**	**Qtz**	**Amp**	**Omp**	**Grt**	**Plg**	**Qtz**
SiO_2	46.08	54.65	39.99	46.23	0.04	0	56.63	99.16	45.09	54.59	40.47	44.68	100.79
TiO_2	0.46	0.16	0.06	0	99.7	54.94	0.02	0	0.42	0.16	0.02	0	0.01
Al_2O_3	12.44	7.02	22.24	37.04	0	0.03	27.83	0.01	12.29	7.05	22.73	35.85	0
Cr_2O_3	0.15	0.02	0.13	0.05	0.41	0.05	0	0.03	0.15	0	0	0	0.01
FeO	10.5	5.32	17.29	0.44	0.21	44.12	0.22	0.2	11.58	5.28	16.55	0.05	0
MgO	13.51	10.93	9.08	0.3	0	0.1	0	0	12.69	10.97	10.66	0.02	0
CaO	11.74	18.38	10.69	0.03	0.13	0	9.64	0	12.27	18.34	9.67	19.23	0
Na_2O	1.96	3.73	0	0.17	0.01	0	6.11	0.01	1.84	3.82	0	0.78	0
K_2O	0.01	0	0	10.85	0	0	0	0	0.02	0	0	0	0
MnO	0.08	0.06	0.28	0	0.02	1.44	0.02	0	0.17	0.08	0.38	0.02	0.01
NiO	0.07	0	0	0.03	0	0.03	0	0.03	0.05	0	0	0.02	0
Total	97	100.27	99.76	95.14	100.52	100.72	100.45	99.43	96.55	100.29	100.48	100.65	100.82

Element	Sample 881							Sample 882				
	Amp	**Omp**	**Grt**	**Ru**	**Ilme**	**Plg**	**Qtz**	**Amp**	**Cpx**	**Grt**	**Mus**	**Ilme**
SiO_2	49.29	53.96	40.56	0	0.04	43.55	99.32	48.27	51.48	40.41	48.99	0
TiO_2	0.24	0.18	0	99.35	54.31	0	0.01	0.3	0.14	0.01	0.02	54.59
Al_2O_3	9.77	7.87	23.2	0.08	0.01	36.65	0	10.15	5.29	23.16	30.24	0.05
Cr_2O_3	0.13	0.13	0.23	0.5	0.06	0	0.02	0.07	0.73	0.12	0.47	0.03
FeO	6.92	2.53	16.51	0.52	43.03	0.05	0.02	8.68	4.98	16.57	1.33	40.98
MgO	16.89	12.3	10.49	0.01	1.83	0	0.02	15.56	12.59	11.35	2.49	0.13
CaO	12.1	19.94	9.55	0.09	0	19.75	0.01	11.86	23.62	8.23	0.01	0.06
Na_2O	1.49	2.97	0	0.08	0.04	0.33	0	1.27	0.72	0.02	0.07	0
K_2O	0	0	0.01	0.01	0	0.01	0	0.01	0	0	11.32	0
MnO	0.11	0.03	0.3	0.03	0.59	0	0	0.1	0.16	0.32	0.02	4.96
NiO	0.05	0.13	0	0.02	0	0	0	0.03	0.04	0.03	0.02	0
Total	96.98	100.04	100.85	100.7	99.91	100.34	99.4	96.31	99.74	100.21	94.98	100.79

Amp: amphibole; Omp: omphacite; Cpx: clinopyroxene; Grt: garnet; Mus: muscovite; Ru: rutile; Ilme: ilmenite; Plg: plagioclase; Qtz: quartz.

Based on the chemical composition of the analyzed minerals and the calculation of the temperature conditions of the samples using geothermometry [75,76], the samples were found to be equilibrated at a temperature of ~750 °C. The equilibrium temperatures of samples are presented in Table 1.

4.3. Lattice-Preferred Orientations of Minerals

The amphibole LPOs are shown in Figure 5, and the strengths of the LPOs of the samples are described in Table 3. For amphibole in retrograded eclogites with relatively little retrogression (samples 880, 881, and 885), the <001> axes of amphibole were strongly aligned subparallel to lineation (L), with a weak girdle distribution subparallel to foliation (S). The amphibole (010) poles were strongly aligned subnormal to foliation, and the amphibole (110) poles formed a girdle distribution subnormal to lineation. The most retrograded eclogite (sample 882) showed that the amphibole <001> axes were strongly aligned subparallel to lineation, with a girdle distribution subparallel to foliation (S), but both amphibole (010) and (110) poles were weakly aligned subnormal to foliation (Figure 5).

The omphacite LPOs are shown in the lower part of Figure 5, and the strengths of the LPOs of the samples are listed in Table 3. Omphacites in samples 880, 881, and 885 showed that the <001> axes were strongly aligned subparallel to lineation, with a girdle distribution subparallel to foliation, and the (010) poles were strongly aligned subnormal to foliation. This omphacite alignment is known as the S-type omphacite LPO [61]. The most retrograded sample 882 contained little clinopyroxene, and the number of clinopyroxene grains in the pole figure was too small (<150 grains) to say LPO [74]. The pole figure did not provide a reliable indication.

The garnet and plagioclase LPOs are shown in Figure 6. They showed a weak LPO, which was considerably dispersed compared to the amphibole and omphacite LPO. The garnet LPO was almost random, independent of the degree of retrogression. In the case of the plagioclase LPO, two samples (885 and 880) showed (010) poles aligned subparallel to lineation.

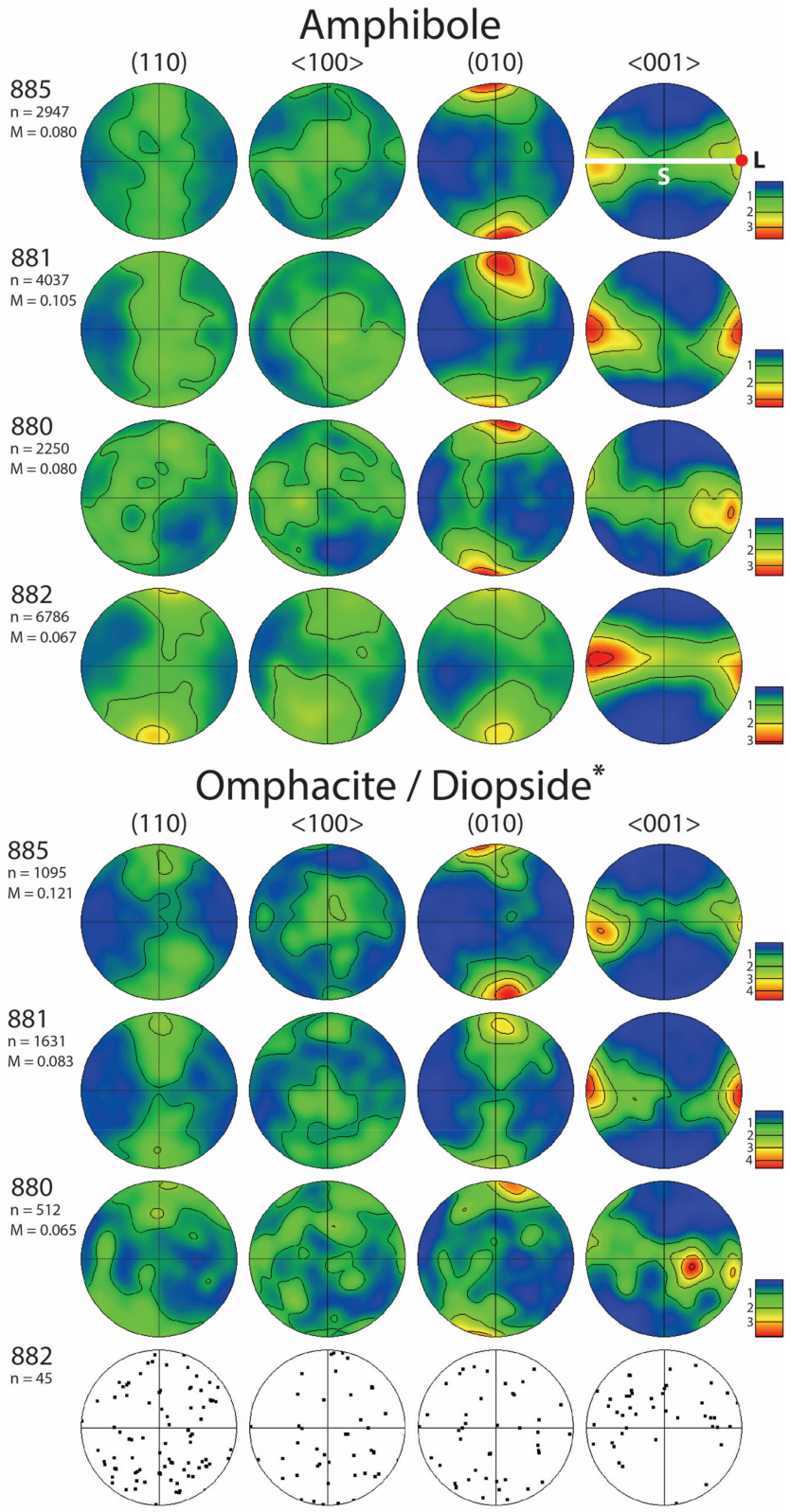

Figure 5. Amphibole and omphacite pole figures (PFs). PFs are presented in the lower hemisphere using an equal area projection. S indicates foliation, and L indicates lineation. Fabric strength of the mineral is shown as the M-index (M). A half scatter width of 20° was used. The color coding (different for each sample) refers to the density of data points, and contours are shown in multiples of uniform distribution. n: number of grains. * Diopside for sample 882.

Table 3. Fabric strength of samples.

Sample	Fabric Strength [a]			
	Amp	Omp	Grt	Plag
885	0.08	0.121	0.018	0.049
881	0.105	0.083	0.016	0.043
880	0.08	0.065	0.045	0.048
882	0.067	-	0.022	0.06

Amp: amphibole; Omp: omphacite; Grt: garnet; Plag: plagioclase. [a] Fabric strength was calculated as the M-index (Skemer et al. [74]).

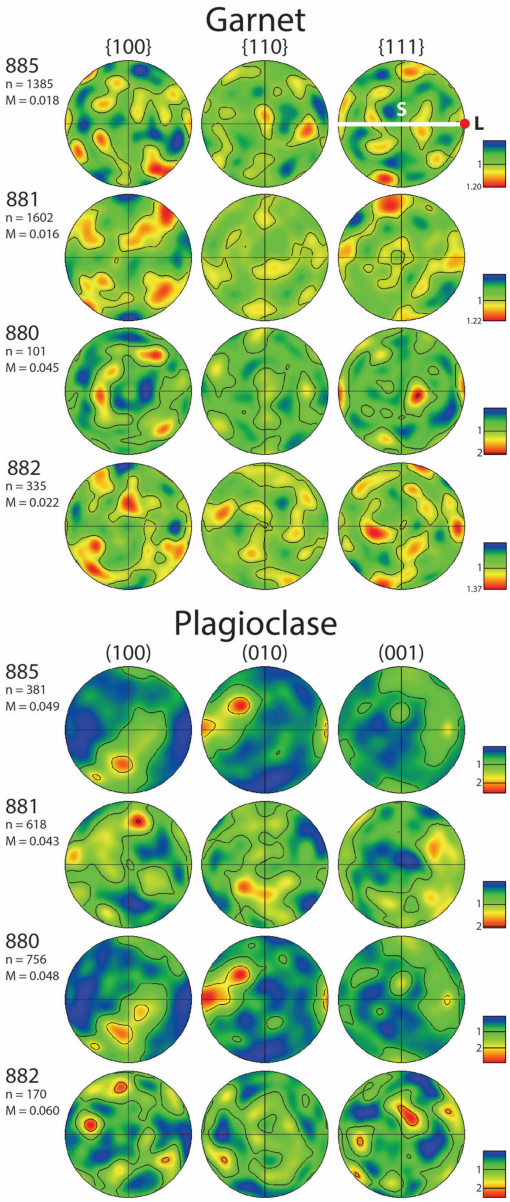

Figure 6. Pole figures (PFs) of garnet and plagioclase. PFs are presented in the lower hemisphere using an equal area projection. S indicates foliation, and L indicates lineation. Fabric strength of the mineral is shown as the M-index (M). A half scatter width of 20° was used. The color coding refers (different for each sample) to the density of data points (n), and contours are shown in multiples of uniform distribution. n: number of grains.

4.4. Misorientation between Amphibole and Omphacite

The misorientation angles between omphacite and amphibole in direct contact with omphacite were measured and are shown in Figure 7. The misorientation angles were significantly low—lower than 3° in both boundaries between omphacite grains, and amphibole in direct contact with omphacite (Figure 7a–c, <0.5°) and the boundary between omphacite and amphibole, which were trapped and surrounded by omphacite (Figure 7d–f, <2°). The symplectites in Figure 7 consist of omphacite, amphibole, diopside, and plagioclase, which were confirmed by measuring the chemical compositions of minerals using the electron probe micro analyzer installed at the National Center for Inter-University Research Facilities at Seoul National University, South Korea.

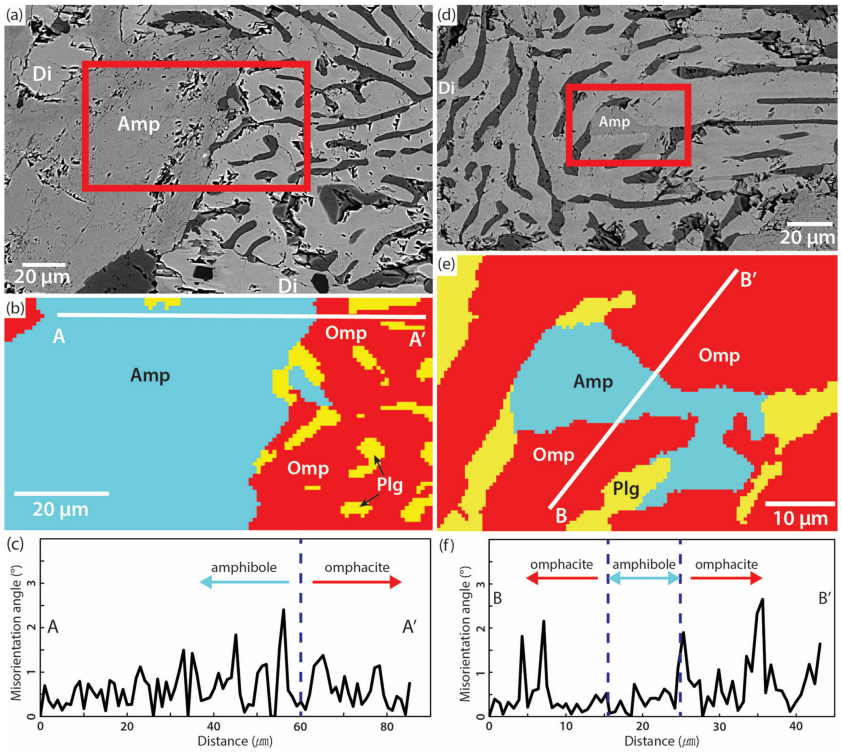

Figure 7. (**a**) and (**d**) Back-scattered electron image of amphibole and directly contacting omphacite symplectite in sample 885; (**b**) and (**e**) EBSD phase map of the area located in the red rectangle in (**a**) and (**d**); and (**c**) and (**f**) misorientation angle distribution spectra along A–A′ in (**b**) and B–B′ in (**e**). Vertical dashed lines indicate the phase boundary between amphibole and omphacite. Omp: omphacite; Amp: amphibole; Di: diopside; Plg: plagioclase.

4.5. Seismic Velocity and Anisotropy

The seismic velocities and anisotropies of the samples are summarized in Table 4. The seismic velocity and anisotropy of the samples are shown in the stereonet for the single-mineral amphibole, omphacite, and garnet and for the whole rock consisting of all minerals, including minor minerals such as plagioclase and ilmenite (Figures 8–10). In the case of amphibole, P-wave velocity (V_P) was in the range of 6.59 to 7.09 km/s, and P-wave anisotropy (AV_P) was in the range of 3.7% to 7.3%, whereas the maximum S-wave anisotropy (max. AV_S) was in the range of 2.72% to 3.61%. In the case of omphacite, the V_P of omphacite was in the range of 8.31 to 8.54 km/s, which is faster than that of amphibole. However, the AV_P of omphacite was in the range of 2.1% to 2.6% and the maximum AV_S was in the range of 1.23% to 1.56%, which is smaller than that of amphibole. In the case of garnet, V_P was the fastest among the minerals, ranging from 9.31 to 9.34 km/s. However, garnet AV_P and maximum AV_S were the smallest compared to other minerals, ranging from 0.1% to 0.3% and 0.16% to 0.55%, respectively (Table 4, Figure 9).

Table 4. Seismic velocity and anisotropy of minerals in samples.

Sample	Amphibole				Omphacite/Diopside *			
	V_P (km/s)	V_S (km/s)	AV_P (%)	Max. AV_S (%)	V_P (km/s)	V_S (km/s)	AV_P (%)	Max. AV_S (%)
885	6.71–6.97	3.66–3.79	3.7	3.28	8.31–8.53	4.85–4.92	2.6	1.41
881	6.67–7.02	3.64–3.79	5.2	3.61	8.36–8.54	4.84–4.92	2.1	1.56
880	6.71–6.97	3.60–3.77	3.8	3.21	8.36–8.53	4.84–4.91	2.1	1.23
882	6.59–7.09	3.65–3.76	7.3	2.72	7.99–8.13	4.66–4.75	1.7	1.68
Sample	**Garnet**				**Whole Rock**			
	V_P (km/s)	V_S (km/s)	AV_P (%)	Max. AV_S (%)	V_P (km/s)	V_S (km/s)	AV_P (%)	Max. AV_S (%)
885	9.32–9.33	5.49–5.50	0.1	0.16	7.57–7.66	4.36–4.44	1.2	1.57
881	9.31–9.33	5.48–5.50	0.2	0.31	7.36–7.55	4.12–4.21	2.6	1.87
880	9.31–9.34	5.47–5.51	0.3	0.55	6.90–7.05	3.84–3.90	2.1	1.40
882	9.31–9.33	5.48–5.51	0.2	0.35	6.70–7.16	3.73–3.83	6.6	2.46

V_P: P-wave velocity; V_S: S-wave velocity; AV_P: anisotropy of P-wave velocity; max. AV_S: maximum anisotropy of S-wave velocity. * Diopside for sample 882.

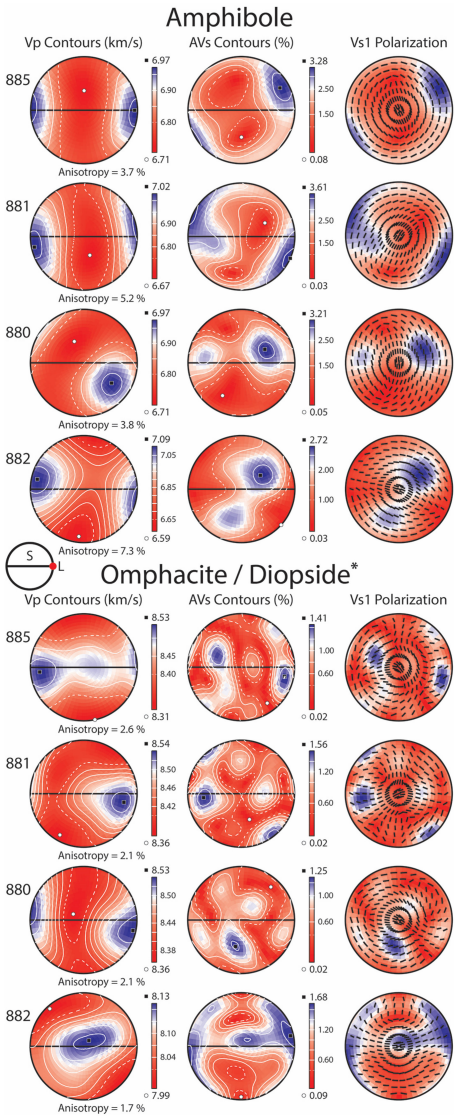

Figure 8. Seismic velocity and anisotropy of amphibole and omphacite. P-wave velocity (V_P) and seismic anisotropy of S-wave (AV_S) are shown. V_S1 polarization indicates the polarization direction of the fast shear wave (V_S1). S and L represent foliation and lineation, respectively. * Diopside for sample 882.

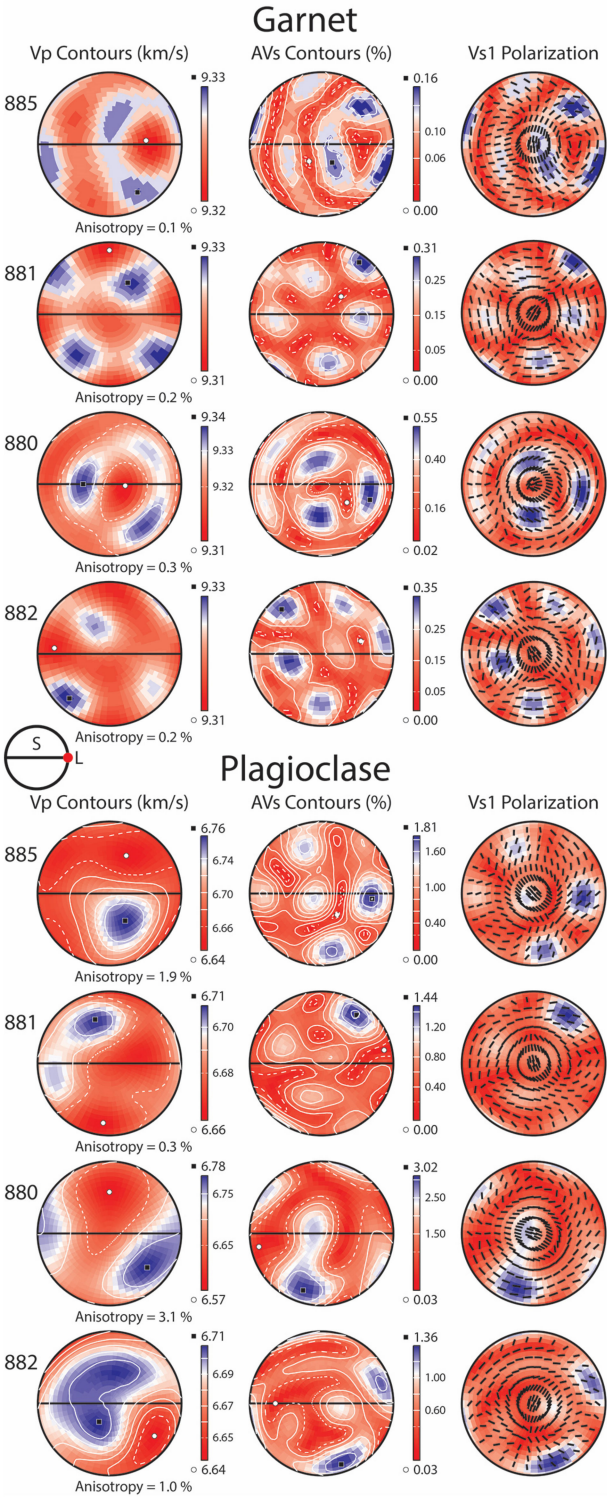

Figure 9. Seismic velocity and anisotropy of garnet and plagioclase. P-wave velocity (V_P) and seismic anisotropy of S-wave (AV_S) are shown. V_S1 polarization indicates the polarization direction of the fast shear wave (V_S1). S and L represent foliation and lineation, respectively.

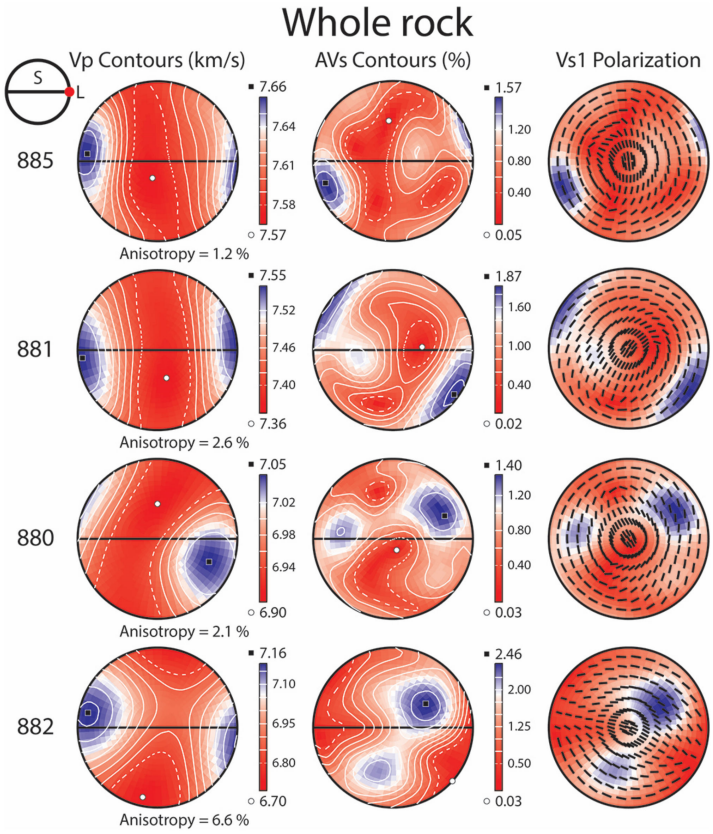

Figure 10. Seismic velocity and anisotropy of whole-rock P-wave velocity (V_P) and seismic anisotropy of S-wave (AV_S) are shown. V_S1 polarization indicates the polarization direction of the fast shear wave (V_S1). S and L represent foliation and lineation, respectively.

The seismic velocity and anisotropy of whole rock showed a value between the seismic velocity and anisotropy of omphacite and amphibole. The V_P of whole rock was in the range of 6.70 to 7.66 km/s, AV_P was in the range of 1.2% to 6.6%, and the maximum AV_S of whole rock was in the range of 1.40% to 2.46%. The seismic velocity and anisotropy profile of whole rock (Figure 10, color-coded and contour lines in pole figures) were much more similar to those of amphibole than those of other minerals (Figures 8 and 9).

4.6. Reflection Coefficient of Samples

The reflection coefficient (R_C) of the boundaries between the studied retrograded eclogites and other rocks in subduction zones is shown in Table 5. The R_C of the boundary between serpentinites and the most retrograded eclogite (sample 882) was in the range of 0.024 to 0.147. The R_C of the boundary between blueschists and the most retrograded eclogite was in the range of 0.011 to 0.05. In addition, the R_C of the boundary between dunite and the most retrograded eclogite was in the range of 0.060 to 0.092. Finally, the R_C of the boundary between peridotites and the most retrograded eclogite was in the range of 0.067 (for amphibole peridotite) to 0.129 (for garnet peridotite). Furthermore, the maximum R_C (R_C = 0.204) was observed at the contact boundary between the serpentinized peridotite [97] and relatively fresh eclogite (sample 885), and the minimum R_C (R_C = 0.002) was observed at the contact boundary between dunite [91] and relatively fresh eclogite.

Table 5. Reflection coefficient (R_C) of the contact boundary between the studied eclogites and other rocks.

Other Rocks	Sample 882 *	Sample 880	Sample 881	Sample 885 +
LT serpentinized peridotite (OHM-B) [a]	0.147	0.161	0.192	0.204
HT serpentinized peridotite (OHM-C) [a]	0.081	0.095	0.126	0.139
Serpentinite [b]	0.049	0.064	0.096	0.108
Glaucophane schist (Ph) [c]	0.041	0.056	0.087	0.100
LT serpentinized peridotite (HPS-J) [a]	0.041	0.055	0.087	0.099
Felsic blueschist [d]	0.026	0.040	0.072	0.084
Epidote blueschist (Gln:Ep = 94:6) [e]	0.011	0.004	0.004	0.048
Lawsonite blueschist (Gln:Lws = 91:9) [e]	0.019	0.004	0.028	0.040
Mafic blusechist [d]	0.019	0.004	0.027	0.039
Epidote blueschist (Gln:Ep = 26:74) [e]	0.021	0.007	0.025	0.037
HT serpentinized peridotite (HPS-I) [a]	0.024	0.009	0.023	0.035
Harzburgite + Melt [f]	0.024	0.009	0.023	0.035
Glaucophane schist (Ep) [c]	0.033	0.019	0.013	0.025
Lawsonite blueschist (Gln: Lws = 75:25) [e]	0.035	0.020	0.012	0.024
Chlorite peridotite [g]	0.044	0.029	0.003	0.015
Lawsonite blueschist [h]	0.050	0.035	0.003	0.009
Harzburgite + Dunite [f]	0.051	0.036	0.005	0.008
Harzburgite [f]	0.053	0.038	0.007	0.006
Dunite [f]	0.060	0.046	0.014	0.002
100% olivine [i]	0.060	0.046	0.014	0.002
Ol 70% + OPX 20% + CPX 10% [i]	0.067	0.052	0.021	0.008
Amphibole peridotite [j]	0.067	0.052	0.021	0.008
Ol 50% + OPX 30% + CPX 20% [i]	0.073	0.059	0.027	0.015
Dunite (NJ437-1) [i]	0.080	0.065	0.003	0.021
Lherzolite [k]	0.080	0.065	0.033	0.021
Dunite [l]	0.080	0.065	0.033	0.021
Lherzolite [m]	0.083	0.068	0.037	0.024
Spinel peridotite [n]	0.089	0.074	0.043	0.030
Lherzolite (NJ437-8) [i]	0.092	0.077	0.046	0.033
Dunite [m]	0.092	0.077	0.046	0.033
Lawsonite eclogite [o]	0.104	0.090	0.058	0.046
Garnet peridotite [p]	0.105	0.090	0.059	0.046
Garnet peridotite (150-4) [q]	0.110	0.096	0.064	0.052
Garnet peridotite [r]	0.112	0.098	0.066	0.054
Garnet peridotite (160-9) [q]	0.129	0.115	0.083	0.071

* Sample 882 is the most retrograded eclogite. + Sample 885 is the relatively fresh eclogite. [a] Watanabe et al. [97]; [b] Jung [95]; [c] Ha et al. [100]; [d] Cao et al. [98]; [e] Kim et al. [86]; [f] Tommasi et al. [91]; [g] Kim and Jung [85]; [h] Cao and Jung [8]; [i] Michibayashi et al. [93]; [j] Kang and Jung [84]; [k] Tommasi et al. [92]; [l] Cao et al. [99]; [m] Tommasi et al. [90]; [n] Jung et al. [94]; [o] Kim et al. [17]; [p] Skemer et al. [87]; [q] Xu et al. [89]; [r] Wang et al. [88]. LT: low temperature; HT: high temperature; Ph: phengite; Gln: glaucophane; Ep: epidote; Lws: lawsonite; Ol: olivine; OPX: orthopyroxene; CPX: clinopyroxene.

5. Discussion

5.1. Lattice-Preferred Orientations of Minerals

Omphacite in retrograded eclogites (samples 880, 881, and 885) from Xitieshan, northwestern China, showed that the <001> axes are strongly aligned subparallel to lineation, with a girdle distribution subparallel to foliation, and the (010) poles are strongly aligned subnormal to foliation. This is called S-type omphacite LPO [61]. The observed S-type omphacite LPOs were consistent with those reported in previous studies [8,22]. The S-type omphacite LPO has been reported in eclogites from the eastern Alps [103] and Cabo Ortegal eclogites from northwestern Spain [104].

Amphibole in retrograded eclogites from Xitieshan, northwest China, showed that the amphibole (010) poles were aligned subnormally to foliation, and the maximum concentration of amphibole <001> axes were aligned subparallel to lineation, which is referred to as type V amphibole LPO. Previously, four other types of amphibole LPOs have been reported in both naturally and experimentally deformed amphibole [12,18,36]. The type V amphibole LPO in this study is different from the amphibole LPOs (types I, II, III, and IV)

reported previously by high-pressure experimental studies. Similar amphibole LPOs to type V LPO have been reported only in naturally deformed amphibole from the Malpica–Tui allochthonous complex, northwestern Spain, and Cabo Ortegal, Spain [44,59], and in retrograded eclogites from the Sanbagawa metamorphic belt, central Shikoku, southwestern Japan [60]. To verify that there was no error in the reference frame (X: lineation, Z: normal to foliation) of samples in our study, the aspect ratios of amphibole and omphacite in the XZ, YZ, and XY planes were determined and compared (Table 1). Grains on the XZ plane were more elongated compared to those on the other planes. This result indicates that the reference frame is correct.

The amphibole LPO (type V) in the studied samples (samples 880, 881, and 885) has only been reported in retrograded eclogites, and the amphibole LPO was similar to that of omphacite in the same samples (Figure 5). The lack of intracrystalline deformation in amphibole indicates that the samples were not deformed after the retrogression of eclogite (Figure 3b,d). In addition, comparison of the misorientation angle between amphibole and the contacting omphacite (Figure 7) showed small angles in both the contact boundary (<2°) and the grain itself (<2.5°), suggesting that type V amphibole LPOs are strongly affected by omphacite LPOs [105,106]. Our results indicate that the amphibole LPO is formed due to the topotactic growth of amphibole during the retrogression of eclogite. Previous studies have also reported that amphibole LPOs are similar to those of omphacite in the same sample, and they suggested that amphibole is formed due to the topotactic growth during retrogression of eclogite [44,59,60].

5.2. Seismic Velocity, Anisotropy, and Reflection Coefficient (R_C)

The amphibole P-wave velocity (V_P) was slow (in the range of 6.59 to 7.09 km/s), and amphibole P-wave anisotropy (AV_P) was large (in the range of 3.7% to 7.3%) (Table 4). The amphibole S-wave velocity (V_S) was also slow (in the range of 3.64 to 3.79 km/s) and amphibole S-wave anisotropy (max. AV_S) large (in the range of 2.72% to 3.61%). When the omphacite seismic velocity and anisotropy were compared with those of amphibole, the seismic velocity of omphacite was much faster than that of amphibole in both P- and S-waves, but the seismic anisotropy of omphacite was much smaller than that of amphibole in both P- and S-waves (Table 4). This is consistent with previous studies on the seismic velocity and anisotropy of these minerals in eclogites [32,107] and the seismic velocity and anisotropy analysis of mineral mixtures in eclogite [22].

The garnet P-wave velocity was the fastest in the studied samples, whereas the amphibole P-wave velocity was the slowest. The P-wave and S-wave anisotropies of garnet were the slowest in the samples, similar to previous studies [22]. The trends in seismic velocity and anisotropy of whole retrograded eclogites (color coded in pole figures in Figure 10) were similar to those of amphibole (Figure 8). This result indicates that the seismic properties of retrograded eclogites are strongly affected by the seismic properties of amphibole due to the high fraction of amphibole (33–91.5%) in retrograded eclogites.

When the seismic velocity and anisotropy of relatively fresh eclogite (sample 885) were compared with those of the most retrograded eclogite (sample 882), the P-wave velocity decreased with increasing retrogression (Figures 8–10 and Table 4), but the P- and S-wave anisotropies increased with increasing retrogression (Figures 8–10 and Table 4). This result indicates that when eclogite increases to the eclogite instability zone and gets retrograded, the seismic velocity of retrograded eclogite decreases, but the seismic anisotropy of retrograded eclogite increases.

The R_C of the studied samples was in the range of 0.002 to 0.204 (Table 5). The contact boundary between relatively fresh eclogite and serpentinized peridotites showed a high R_C (up to 0.204), which was high enough to reflect the seismic wave. However, at the contact boundary between the studied eclogites and the dunites and blueschists, the R_C was small (0.002–0.05), independent of the degree of retrogression of eclogite (Table 5). A small R_C indicates that the seismic wave reflects little at this boundary, and the seismic wave reflected by this boundary is difficult to detect [6].

In Figure 11, the R_C between various rocks and the studied eclogites is compared with the P-wave velocity. In the case of serpentinized peridotites, which have low V_P (V_P < 6.8 km/s), the R_C was high for the contact boundary with relatively fresh eclogite (sample 885), indicating that the boundary between serpentinized peridotites and the relatively fresh eclogites reflects a large seismic wave, resulting in this boundary being easily detected compared to the other contact boundaries of rocks. In contrast, in the case of dry mantle rocks (spinel peridotites and garnet peridotites), which have a high V_P (V_P > 7.5 km/s), the R_C was high for the contact boundary with the most retrograded eclogite (sample 882). This result indicates that the contact boundary between dry mantle rocks and the most retrograded eclogite reflects more seismic waves, resulting in the boundary being easily detected compared to the other contact boundaries of rocks, similar to the contact boundary between serpentinized peridotites and relatively fresh eclogite. However, in the case of blueschists, which have an intermediate V_P (6.8 km/s < V_P < 7.5 km/s), the R_C was low for the contact boundary with the studied eclogites, whether eclogites were retrograded or not, indicating that the boundaries between blueschists and eclogites reflected little seismic waves, independent of the degree of retrogression of eclogite, indicating that these boundaries may be difficult to detect.

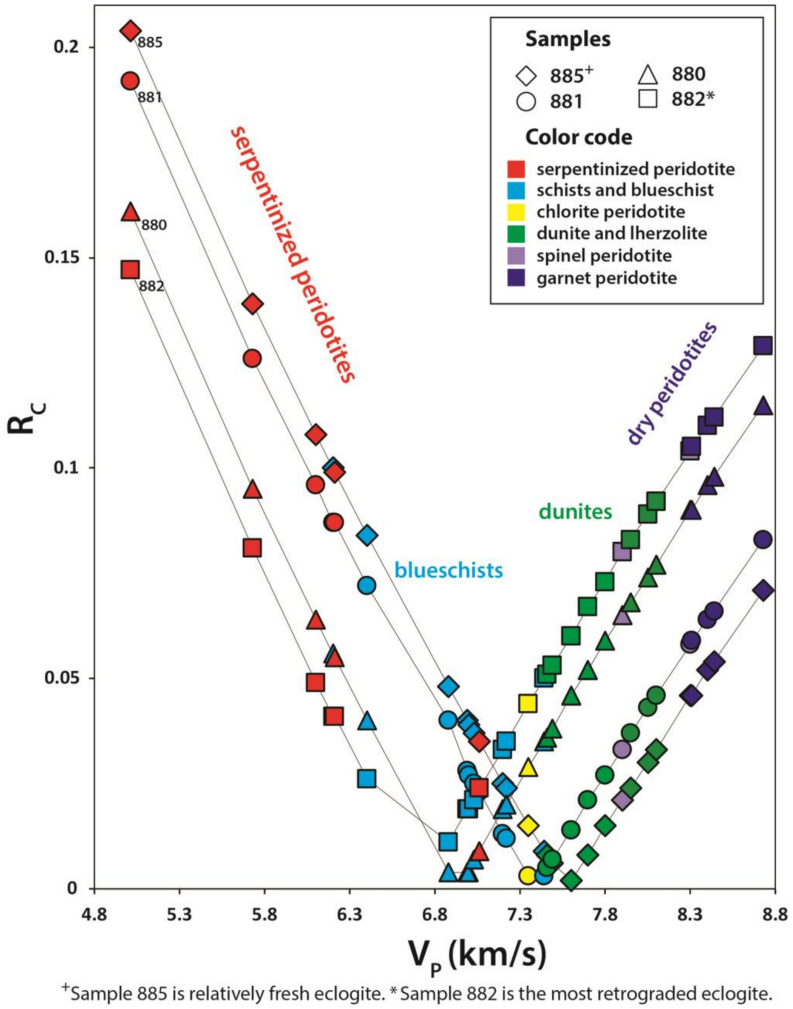

Figure 11. Relationship between P-wave velocity (V_P) of a surrounding rock and reflection coefficient (R_C) of the contact boundary between the studied retrograded eclogite and the surrounding rock (Table 5).

6. Conclusions

The LPOs of minerals in retrograded eclogites from Xitieshan, northwestern China, were studied to understand the seismic anisotropies and seismic reflection coefficients of the rocks that are in contact with other surrounding rocks. The amphibole LPOs in the retrograded eclogites were mostly similar to omphacite LPOs. The low misorientation angle between amphibole in direct contact with omphacite suggests that the amphibole LPO is formed due to topotactic growth of amphibole during the retrogression process of eclogites. There was a lack of intracrystalline deformation features in amphibole, such as undulose extinction and subgrains, indicating that there might have been little deformation after the retrogression of eclogites.

The seismic properties of retrograded eclogites were more severely affected by amphibole than by other minerals due to the high fraction of amphibole (33–91.5%) in retrograded eclogites. During the retrogression process of eclogites, the seismic velocity slowed and the seismic anisotropy increased. R_C, which was calculated using the V_P of minerals, showed that the contact boundaries between relatively fresh eclogite and hydrated mantle rocks, such as serpentinized peridotites, showed high R_C, indicating that these contact boundaries can be easily detected using the reflected seismic wave, but the contact boundaries between dunites or blueschists and eclogites showed low R_C, independent of the degree of retrogression. This indicates that these contact boundaries are expected to be difficult to detect using the reflected seismic wave.

Author Contributions: Conceptualization, H.J.; methodology, J.L. and H.J.; software, J.L.; validation, J.L. and H.J.; formal analysis, J.L.; investigation, J.L.; resources, J.L. and H.J.; data curation, J.L.; writing—original draft preparation, J.L.; writing—review and editing, J.L. and H.J.; visualization, J.L.; supervision, H.J.; project administration, H.J.; funding acquisition, H.J. All authors have read and agreed to the published version of the manuscript.

Funding: This research was supported by a grant to H.J. from the Korea Meteorological Administration Research Development Program (KMI2019-00110).

Institutional Review Board Statement: Not applicable.

Informed Consent Statement: Not applicable.

Data Availability Statement: Not applicable.

Acknowledgments: The authors are grateful to the anonymous reviewers for constructive comments and corrections.

Conflicts of Interest: The authors declare no conflict of interest.

References

1. Savage, M.K. Seismic anisotropy and mantle deformation: What have we learned from shear wave splitting? *Rev. Geophys.* **1999**, *37*, 65–106. [CrossRef]
2. Long, M.D.; Silver, P.G. The subduction zone flow field from seismic anisotropy: A global view. *Science* **2008**, *319*, 315–318. [CrossRef] [PubMed]
3. Stern, R.J. Subduction zones. *Rev. Geophys.* **2002**, *40*, 3-1–3-38. [CrossRef]
4. Cao, Y.; Jung, H.; Song, S. Microstructures and petro-fabrics of lawsonite blueschist in the North Qilian suture zone, NW China: Implications for seismic anisotropy of subducting oceanic crust. *Tectonophysics* **2014**, *628*, 140–157. [CrossRef]
5. Ábalos, B.; Fountain, D.M.; Ibarguchi, J.I.G.; Puelles, P. Eclogite as a seismic marker in subduction channels: Seismic velocities, anisotropy, and petrofabric of Cabo Ortegal eclogite tectonites (Spain). *Geol. Soc. Am. Bull.* **2011**, *123*, 439–456. [CrossRef]
6. Bascou, J.; Barruol, G.; Vauchez, A.; Mainprice, D.; Egydio-Silva, M. EBSD-measured lattice-preferred orientations and seismic properties of eclogites. *Tectonophysics* **2001**, *342*, 61–80. [CrossRef]
7. Ben Ismail, W.; Mainprice, D. An olivine fabric database: An overview of upper mantle fabrics and seismic anisotropy. *Tectonophysics* **1998**, *296*, 145–157. [CrossRef]
8. Cao, Y.; Jung, H. Seismic properties of subducting oceanic crust: Constraints from natural lawsonite-bearing blueschist and eclogite in Sivrihisar Massif, Turkey. *Phys. Earth Planet. Inter.* **2016**, *250*, 12–30. [CrossRef]
9. Godard, G.; van Roermund, H.L.M. Deformation-induced clinopyroxene fabrics from eclogites. *J. Struct. Geol.* **1995**, *17*, 1425–1443. [CrossRef]

10. Ji, S.; Saruwatari, K.; Mainprice, D.; Wirth, R.; Xu, Z.; Xia, B. Microstructures, petrofabrics and seismic properties of ultra high-pressure eclogites from Sulu region, China: Implications for rheology of subducted continental crust and origin of mantle reflections. *Tectonophysics* **2003**, *370*, 49–76. [CrossRef]
11. Ji, S.; Wang, Q.; Xia, B. P-wave velocities of polymineralic rocks: Comparison of theory and experiment and test of elastic mixture rules. *Tectonophysics* **2003**, *366*, 165–185. [CrossRef]
12. Jung, H. Crystal preferred orientations of olivine, orthopyroxene, serpentine, chlorite, and amphibole, and implications for seismic anisotropy in subduction zones: A review. *Geosci. J.* **2017**, *21*, 985–1011. [CrossRef]
13. Jung, H.; Karato, S. Water-induced fabric transitions in olivine. *Science* **2001**, *293*, 1460–1463. [CrossRef]
14. Jung, H.; Katayama, I.; Jiang, Z.; Hiraga, I.; Karato, S. Effect of water and stress on the lattice-preferred orientation of olivine. *Tectonophysics* **2006**, *421*, 1–22. [CrossRef]
15. Karato, S.; Jung, H.; Katayama, I.; Skemer, P. Geodynamic significance of seismic anisotropy of the upper mantle: New insights from laboratory studies. *Annu. Rev. Earth Planet. Sci.* **2008**, *36*, 59–95. [CrossRef]
16. Keppler, R.; Ullemeyer, K.; Behrmann, J.H.; Stipp, M.; Kurzawski, R.M.; Lokajíček, T. Crystallographic preferred orientations of exhumed subduction channel rocks from the Eclogite Zone of the Tauern Window (Eastern Alps, Austria), and implications on rock elastic anisotropies at great depths. *Tectonophysics* **2015**, *647*, 89–104. [CrossRef]
17. Kim, D.; Wallis, S.; Endo, S.; Ree, J.-H. Seismic properties of lawsonite eclogites from the southern Motagua fault zone, Guatemala. *Tectonophysics* **2016**, *677–678*, 88–98. [CrossRef]
18. Ko, B.; Jung, H. Crystal preferred orientation of an amphibole experimentally deformed by simple shear. *Nat. Commun.* **2015**, *6*, 6586. [CrossRef]
19. Lee, J.; Jung, H.; Klemd, R.; Tarling, M.S.; Konopelko, D. Lattice preferred orientation of talc and implications for seismic anisotropy in subduction zones. *Earth Planet. Sci. Lett.* **2020**, *537*, 116178. [CrossRef]
20. Mauler, A.; Burlini, L.; Kunze, K.; Philippot, P.; Burg, J.P. P-wave anisotropy in eclogites and relationship to the omphacite crystallographic fabric. *Phys. Chem. Earth Part A Solid Earth Geod.* **2000**, *25*, 119–126. [CrossRef]
21. Nicolas, A.; Christensen, N.I. Formation of Anisotropy in Upper Mantle Peridotites—A Review. In *Composition, Structure and Dynamics of the Lithosphere-Asthenosphere System*; Fuchs, K., Froidevaux, C., Eds.; American Geophysical Union: Washington, DC, USA, 1987; Volumn 16, pp. 111–123.
22. Park, M.; Jung, H. Relationships between eclogite-facies mineral assemblages, deformation microstructures, and seismic properties in the Yuka terrane, North Qaidam ultrahigh-pressure metamorphic belt, NW China. *J. Geophys. Res. Solid Earth* **2019**, *124*, 13168–13191. [CrossRef]
23. Worthington, J.R.; Hacker, B.R.; Zandt, G. Distinguishing eclogite from peridotite: EBSD-based calculations of seismic velocities. *Geophys. J. Int.* **2013**, *193*, 489–505. [CrossRef]
24. Almqvist, B.S.; Mainprice, D. Seismic properties and anisotropy of the continental crust: Predictions based on mineral texture and rock microstructure. *Rev. Geophys.* **2017**, *55*, 367–433. [CrossRef]
25. Evans, B.W. Phase-relations of epidote-blueschists. *Lithos* **1990**, *25*, 3–23. [CrossRef]
26. Okamoto, K.; Maruyama, S. The high-pressure synthesis of lawsonite in the MORB+H2O system. *Am. Mineral.* **1999**, *84*, 362–373. [CrossRef]
27. Tsujimori, T.; Ernst, W.G. Lawsonite blueschists and lawsonite eclogites as proxies for palaeo-subduction zone processes: A review. *J. Metamorph. Geol.* **2014**, *32*, 437–454. [CrossRef]
28. Wei, C.J.; Clarke, G.L. Calculated phase equilibria for MORB compositions: A reappraisal of the metamorphic evolution of lawsonite eclogite. *J. Metamorph. Geol.* **2011**, *29*, 939–952. [CrossRef]
29. Bhagat, S.S.; Bass, J.D.; Smyth, J.R. Single-crystal elastic properties of omphacite-C2/C by Brillouin spectroscopy. *J. Geophys. Res. Solid Earth* **1992**, *97*, 6843–6848. [CrossRef]
30. Barruol, G.; Mainprice, D. A quantitative-evaluation of the contribution of crustal rocks to the shear-wave splitting of teleseismic SKS waves. *Phys. Earth Planet. Inter.* **1993**, *78*, 281–300. [CrossRef]
31. Christensen, N.I.; Mooney, W.D. Seismic velocity structure and composition of the continental-crust—A global view. *J. Geophys. Res. Solid Earth* **1995**, *100*, 9761–9788. [CrossRef]
32. Shi, F.; Wang, Y.; Xu, H.; Zhang, J. Effects of lattice preferred orientation and retrogression on seismic properties of eclogite. *J. Earth Sci.* **2010**, *21*, 569–580. [CrossRef]
33. Rudnick, R.; Gao, S. Composition of the continental crust. *Treatise Geochem.* **2003**, *3*, 659.
34. Fountain, D.M.; Salisbury, M.H. Exposed cross-sections through the continental-crust—Implications for crustal structure, petrology, and evolution. *Earth Planet. Sci. Lett.* **1981**, *56*, 263–277. [CrossRef]
35. Ji, S.; Shao, T.; Michibayashi, K.; Long, C.; Wang, Q.; Kondo, Y.; Zhao, W.; Wang, H.; Salisbury, M.H. A new calibration of seismic velocities, anisotropy, fabrics, and elastic moduli of amphibole-rich rocks. *J. Geophys. Res. Solid Earth* **2013**, *118*, 4699–4728. [CrossRef]
36. Kim, J.; Jung, H. New Crystal Preferred Orientation of Amphibole Experimentally Found in Simple Shear. *Geophys. Res. Lett.* **2019**, *46*. [CrossRef]
37. Bezacier, L.; Reynard, B.; Bass, J.D.; Wang, J.; Mainprice, D. Elasticity of glaucophane, seismic velocities and anisotropy of the subducted oceanic crust. *Tectonophysics* **2010**, *494*, 201–210. [CrossRef]

38. Cao, Y.; Song, S.G.; Niu, Y.L.; Jung, H.; Jin, Z.M. Variation of mineral composition, fabric and oxygen fugacity from massive to foliated eclogites during exhumation of subducted ocean crust in the North Qilian suture zone, NW China. *J. Metamorph. Geol.* **2011**, *29*, 699–720. [CrossRef]
39. Fountain, D.M.; Boundy, T.M.; Austrheim, H.; Rey, P. Eclogite-facies shear zones—Deep-crustal reflectors. *Tectonophysics* **1994**, *232*, 411–424. [CrossRef]
40. Fujimoto, Y.; Kono, Y.; Hirajima, T.; Kanagawa, K.; Ishikawa, M.; Arima, M. P-wave velocity and anisotropy of lawsonite and epidote blueschists: Constraints on water transportation along subducting oceanic crust. *Phys. Earth Planet. Inter.* **2010**, *183*, 219–228. [CrossRef]
41. Kern, H.; Gao, S.; Jin, Z.M.; Popp, T.; Jin, S.Y. Petrophysical studies on rocks from the Dabie ultrahigh-pressure (UHP) metamorphic belt, Central China: Implications for the composition and delamination of the lower crust. *Tectonophysics* **1999**, *301*, 191–215. [CrossRef]
42. Kern, H.; Jin, Z.M.; Gao, S.; Popp, T.; Xu, Z.Q. Physical properties of ultrahigh-pressure metamorphic rocks from the Sulu terrain, eastern central China: Implications for the seismic structure at the Donghai (CCSD) drilling site. *Tectonophysics* **2002**, *354*, 315–330. [CrossRef]
43. Kim, D.; Katayama, I.; Michibayashi, K.; Tsujimori, T. Rheological contrast between glaucophane and lawsonite in naturally deformed blueschist from Diablo Range, California. *Island Arc.* **2013**, *22*, 63–73. [CrossRef]
44. Llana-Funez, S.; Brown, D. Contribution of crystallographic preferred orientation to seismic anisotropy across a surface analog of the continental Moho at Cabo Ortegal, Spain. *Geol. Soc. Am. Bull.* **2012**, *124*, 1495–1513. [CrossRef]
45. Mookherjee, M.; Bezacier, L. The low velocity layer in subduction zone: Structure and elasticity of glaucophane at high pressures. *Phys. Earth Planet. Inter.* **2012**, *208*, 50–58. [CrossRef]
46. Rudnick, R.L.; Fountain, D.M. Nature and composition of the continental-crust—A lower crustal perspective. *Rev. Geophys.* **1995**, *33*, 267–309. [CrossRef]
47. Sun, S.; Ji, S.; Wang, Q.; Xu, Z.; Salisbury, M.; Long, C. Seismic velocities and anisotropy of core samples from the Chinese Continental Scientific Drilling borehole in the Sulu UHP terrane, eastern China. *J. Geophys. Res. Solid Earth* **2012**, *117*. [CrossRef]
48. Wang, Q.; Burlini, L.; Mainprice, D.; Xu, Z. Geochemistry, petrofabrics and seismic properties of eclogites from the Chinese Continental Scientific Drilling boreholes in the Sulu UHP terrane, eastern China. *Tectonophysics* **2009**, *475*, 251–266. [CrossRef]
49. Zhang, J.; Wang, Y.; Jin, Z. CPO-induced seismic anisotropy in UHP eclogites. *Sci. China Ser. D Earth Sci.* **2008**, *51*, 11–21. [CrossRef]
50. Cooke, D.A.; Schneider, W.A. Generalized linear inversion of reflection seismic data. *Geophysics* **1983**, *48*, 665–676. [CrossRef]
51. Xu, D.; Wang, Y.; Gan, Q.; Tang, J. Frequency-dependent seismic reflection coefficient for discriminating gas reservoirs. *J. Geophys. Eng.* **2011**, *8*, 508–513. [CrossRef]
52. Laubscher, H. The problem of the moho in the Alps. *Tectonophysics* **1990**, *182*, 9–20. [CrossRef]
53. Warner, M.; Morgan, J.; Barton, P.; Morgan, P.; Price, C.; Jones, K. Seismic reflections from the mantle represent relict subduction zones within the continental lithosphere. *Geology* **1996**, *24*, 39–42. [CrossRef]
54. Bass, J.D. Elasticity of grossular and spessartite garnets by Brillouin spectroscopy. *J. Geophys. Res. Solid Earth Planets* **1989**, *94*, 7621–7628. [CrossRef]
55. Díaz Aspiroz, M.; Lloyd, G.E.; Fernández, C. Development of lattice preferred orientation in clinoamphiboles deformed under low-pressure metamorphic conditions. A SEM/EBSD study of metabasites from the Aracena metamorphic belt (SW Spain). *J. Struct. Geol.* **2007**, *29*, 629–645. [CrossRef]
56. Getsinger, A.J.; Hirth, G. Amphibole fabric formation during diffusion creep and the rheology of shear zones. *Geology* **2014**, *42*, 535–538. [CrossRef]
57. Puelles, P.; Gil Ibarguchi, J.I.; Beranoaguirre, A.; Ábalos, B. Mantle wedge deformation recorded by high-temperature peridotite fabric superposition and hydrous retrogression (Limo massif, Cabo Ortegal, NW Spain). *Int. J. Earth Sci.* **2012**, *101*, 1835–1853. [CrossRef]
58. Tatham, D.; Lloyd, G.; Butler, R.; Casey, M. Amphibole and lower crustal seismic properties. *Earth Planet. Sci. Lett.* **2008**, *267*, 118–128. [CrossRef]
59. Puelles, P.; Beranoaguirre, A.; Ábalos, B.; Gil Ibarguchi, J.I.; García de Madinabeitia, S.; Rodríguez, J.; Fernández-Armas, S. Eclogite inclusions from subducted metaigneous continental crust (Malpica-Tui Allochthonous Complex, NW Spain): Petrofabric, geochronology, and calculated seismic properties. *Tectonics* **2017**, *36*, 1376–1406. [CrossRef]
60. Rehman, H.U.; Mainprice, D.; Barou, F.; Yamamoto, H.; Okamoto, K. EBSD-measured crystal preferred orientation of eclogites from the Sanbagawa metamorphic belt, central Shikoku, SW Japan. *Eur. J. Mineral.* **2016**, *28*, 1155–1168. [CrossRef]
61. Zhang, J.F.; Green, H.W.; Bozhilov, K.N. Rheology of omphacite at high temperature and pressure and significance of its lattice preferred orientations. *Earth Planet. Sci. Lett.* **2006**, *246*, 432–443. [CrossRef]
62. Chen, N.S.; Xia, X.P.; Li, X.Y.; Sun, M.; Xu, P.; Liu, X.M.; Wang, X.Y.; Wang, Q.Y. Timing of magmatism of the gneissic-granite plutons along North Qaidam margin and implications for Precambrian crustal accretions: Zircon U-Pb dating and Hf isotope evidences. *Acta Petrol. Sin.* **2007**, *23*, 501–512.
63. Fu, J.; Liang, X.; Zhou, Y.; Wang, C.; Jiang, Y.; Zhong, Y. Geochemistry, zircon U-Pb geochronology and Hf isotopes of granitic rocks in the Xitieshan area, North Qaidam, Northwest China: Implications for Neoproterozoic geodynamic evolutions of North Qaidam. *Precambrian Res.* **2015**, *264*, 11–29. [CrossRef]
64. Zhao, Z.X.; Wei, J.H.; Fu, L.B.; Liang, S.N.; Zhao, S.Q. The Early Paleozoic Xitieshan syn-collisional granite in the North Qaidam ultrahigh-pressure metamorphic belt, NW China: Petrogenesis and implications for continental crust growth. *Lithos* **2017**, *278*, 140–152. [CrossRef]

65. Zhang, J.; Yang, J.; Meng, F.; Wan, Y.; Li, H.; Wu, C. U–Pb isotopic studies of eclogites and their host gneisses in the Xitieshan area of the North Qaidam mountains, western China: New evidence for an early Paleozoic HP–UHP metamorphic belt. *J. Asian Earth Sci.* **2006**, *28*, 143–150.
66. Zhang, C.; Zhang, L.; Bader, T.; Song, S.; Lou, Y. Geochemistry and trace element behaviors of eclogite during its exhumation in the Xitieshan terrane, North Qaidam UHP belt, NW China. *J. Asian Earth Sci.* **2013**, *63*, 81–97. [CrossRef]
67. Zhang, C.; Zhang, L.; van Roermund, H.; Song, S.; Zhang, G. Petrology and SHRIMP U-Pb dating of Xitieshan eclogite, North Qaidam UHP metamorphic belt, NW China. *J. Asian Earth Sci.* **2011**, *42*, 752–767. [CrossRef]
68. Liu, X.; Wu, Y.; Gao, S.; Liu, Q.; Wang, H.; Qin, Z.; Li, Q.; Li, X.-H.; Gong, H. First record and timing of UHP metamorphism from zircon in the Xitieshan terrane: Implications for the evolution of the entire North Qaidam metamorphic belt. *Am. Mineral.* **2012**, *97*, 1083–1093. [CrossRef]
69. Song, S.; Zhang, C.; Li, X.; Zhang, L. HP/UHP metamorphic time of eclogite in the Xitieshan terrane, North Qaidam UHPM belt, NW China. *Acta Petrol. Sin.* **2011**, *27*, 1191–1197.
70. Zhang, C.; Bader, T.; Zhang, L.F.; van Roermund, H. The multi-stage tectonic evolution of the Xitieshan terrane, North Qaidam orogen, western China: From Grenville-age orogeny to early-Paleozoic ultrahigh-pressure metamorphism. *Gondwana Res.* **2017**, *41*, 290–300. [CrossRef]
71. Zhang, J.X.; Yang, J.S.; Mattinson, C.G.; Xu, Z.Q.; Meng, F.C.; Shi, R.D. Two contrasting eclogite cooling histories, North Qaidam HP/UHP terrane, western China: Petrological and isotopic constraints. *Lithos* **2005**, *84*, 51–76. [CrossRef]
72. Panozzo, R. Two-dimensional strain from the orientation of lines in a plane. *J. Struct. Geol.* **1984**, *6*, 215–221. [CrossRef]
73. Park, M.; Jung, H. Analysis of electron backscattered diffraction (EBSD) mapping of geological materials: Precautions for reliably collecting and interpreting data on petro-fabric and seismic anisotropy. *Geosci. J.* **2020**, *24*, 679–687. [CrossRef]
74. Skemer, P.; Katayama, B.; Jiang, Z.T.; Karato, S. The misorientation index: Development of a new method for calculating the strength of lattice-preferred orientation. *Tectonophysics* **2005**, *411*, 157–167. [CrossRef]
75. Krogh Ravna, E.J.; Terry, M.P. Geothermobarometry of UHP and HP eclogites and schists–an evaluation of equilibria among garnet–clinopyroxene–kyanite–phengite–coesite/quartz. *J. Metamorph. Geol.* **2004**, *22*, 579–592. [CrossRef]
76. Ravna, K. The garnet–clinopyroxene Fe2+–Mg geothermometer: An updated calibration. *J. Metamorph. Geol.* **2000**, *18*, 211–219. [CrossRef]
77. Aleksandrov, K.S.; Ryzhova, T.V. The elastic properties of rock forming minerals, pyroxenes and amphiboles. *Bull. Acad. Sci. USSR Geophys. Ser.* **1961**, *871*, 1339–1344.
78. Isaak, D.G.; Ohno, I.; Lee, P.C. The elastic constants of monoclinic single-crystal chrome-diopside to 1,300 K. *Phys. Chem. Miner.* **2006**, *32*, 691–699. [CrossRef]
79. Aleksandrov, K.S. Velocities of elastic waves in minerals at atmospheric pressure and increasing precision of elastic constants by means of EVM. *Izv. Acad. Sci. USSR Geol. Ser.* **1974**, *10*, 15–24.
80. Mainprice, D. A Frotran program to calculate seismic anisotropy from the lattice preferred orientation of minerals. *Comput. Geosci.* **1990**, *16*, 385–393. [CrossRef]
81. McSkimin, H.J.; Andreatch, P., Jr.; Thurston, R.N.L. Elastic moduli of quartz versus hydrostatic pressure at 25 and −195.8 C. *J. Appl. Phys.* **1965**, *36*, 1624–1632. [CrossRef]
82. Weidner, D.J.; Ito, E. Elasticity of MgSiO3 in the ilmenite phase. *Phys. Earth Planet. Inter.* **1985**, *40*, 65–70. [CrossRef]
83. Vaughan, M.T.; Guggenheim, S. Elasticity of muscovite and its relationship to crystal structure. *J. Geophys. Res. Solid Earth* **1986**, *91*, 4657–4664. [CrossRef]
84. Kang, H.; Jung, H. Lattice-preferred orientation of amphibole, chlorite, and olivine found in hydrated mantle peridotites from Bjørkedalen, southwestern Norway, and implications for seismic anisotropy. *Tectonophysics* **2019**, *750*, 137–152. [CrossRef]
85. Kim, D.; Jung, H. Deformation microstructures of olivine and chlorite in chlorite peridotites from Almklovdalen in the Western Gneiss Region, SW Norway and implications for seismic anisotropy. *Int. Geol. Rev.* **2015**. [CrossRef]
86. Kim, D.; Katayama, I.; Michibayashi, K.; Tsujimori, T. Deformation fabrics of natural blueschists and implications for seismic anisotropy in subducting oceanic crust. *Phys. Earth Planet. Inter.* **2013**, *222*, 8–21. [CrossRef]
87. Skemer, P.; Katayama, I.; Karato, S.I. Deformation fabrics of the Cima di Gagnone peridotite massif, Central Alps, Switzerland: Evidence of deformation at low temperatures in the presence of water. *Contrib. Mineral. Petrol.* **2006**, *152*, 43–51. [CrossRef]
88. Wang, Y.F.; Zhang, J.F.; Shi, F. The origin and geophysical implications of a weak C-type olivine fabric in the Xugou ultrahigh pressure garnet peridotite. *Earth Planet. Sci. Lett.* **2013**, *376*, 63–73. [CrossRef]
89. Xu, Z.Q.; Wang, Q.; Ji, S.C.; Chen, J.; Zeng, L.S.; Yang, J.S.; Chen, F.Y.; Liang, F.H.; Wenk, H.R. Petrofabrics and seismic properties of garnet peridotite from the UHP Sulu terrane (China): Implications for olivine deformation mechanism in a cold and dry subducting continental slab. *Tectonophysics* **2006**, *421*, 111–127. [CrossRef]
90. Tommasi, A.; Godard, M.; Coromina, G.; Dautria, J.-M.; Barsczus, H. Seismic anisotropy and compositionally induced velocity anomalies in the lithosphere above mantle plumes: A petrological and microstructural study of mantle xenoliths from French Polynesia. *Earth Planet. Sci. Lett.* **2004**, *227*, 539–556. [CrossRef]
91. Tommasi, A.; Vauchez, A.; Godard, M.; Belley, F. Deformation and melt transport in a highly depleted peridotite massif from the Canadian Cordillera: Implications to seismic anisotropy above subduction zones. *Earth Planet. Sci. Lett.* **2006**, *252*, 245–259. [CrossRef]
92. Tommasi, A.; Vauchez, A.; Ionov, D.A. Deformation, static recrystallization, and reactive melt transport in shallow subcontinental mantle xenoliths (Tok Cenozoic volcanic field, SE Siberia). *Earth Planet. Sci. Lett.* **2008**, *272*, 65–77. [CrossRef]

93. Michibayashi, K.; Kusafuka, Y.; Satsukawa, T.; Nasir, S.J. Seismic properties of peridotite xenoliths as a clue to imaging the lithospheric mantle beneath NE Tasmania, Australia. *Tectonophysics* **2012**, *522*, 218–223. [CrossRef]
94. Jung, S.; Jung, H.; Austrheim, H. Characterization of olivine fabrics and mylonite in the presence of fluid and implications for seismic anisotropy and shear localization. *Earth Planets Space* **2014**, *66*. [CrossRef]
95. Jung, H. Seismic anisotropy produced by serpentine in mantle wedge. *Earth Planet. Sci. Lett.* **2011**, *307*, 535–543. [CrossRef]
96. Katayama, I.; Hirauchi, H.; Michibayashi, K.; Ando, J. Trench-parallel anisotropy produced by serpentine deformation in the hydrated mantle wedge. *Nature* **2009**, *461*, 1114–1117. [CrossRef]
97. Watanabe, T.; Kasami, H.; Ohshima, S. Compressional and shear wave velocities of serpentinized peridotites up to 200 MPa. *Earth, Planets Space* **2007**, *59*, 233–244. [CrossRef]
98. Cao, Y.; Jung, H.; Song, S.G. Petro-fabrics and seismic properties of blueschist and eclogite in the North Qilian suture zone, NW China: Implications for the low-velocity upper layer in subducting slab, trench-parallel seismic anisotropy, and eclogite detectability in the subduction zone. *J. Geophys. Res. Solid Earth* **2013**, *118*, 3037–3058. [CrossRef]
99. Cao, Y.; Jung, H.; Song, S. Seismic anisotropies of the Songshugou peridotites (Qinling orogen, central China) and their seismic implications. *Tectonophysics* **2018**, *722*, 432–446. [CrossRef]
100. Ha, Y.; Jung, H.; Raymond, L.A. Deformation fabrics of glaucophane schists and implications for seismic anisotropy: The importance of lattice preferred orientation of phengite. *Int. Geol. Rev.* **2018**, 1–18. [CrossRef]
101. Locock, A.J. An Excel spreadsheet to classify chemical analyses of amphiboles following the IMA 2012 recommendations. *Comput. Geosci.* **2014**, *62*, 1–11. [CrossRef]
102. Hawthorne, F.C.; Oberti, R.; Harlow, G.E.; Maresch, W.V.; Martin, R.F.; Schumacher, J.C.; Welch, M.D. Nomenclature of the amphibole supergroup. *Am. Mineral.* **2012**, *97*, 2031–2048. [CrossRef]
103. Neufeld, K.; Ring, U.; Heidelbach, F.; Dietrich, S.; Neuser, R. Omphacite textures in eclogites of the Tauern Window: Implications for the exhumation of the Eclogite Zone, Eastern Alps. *J. Struct. Geol.* **2008**, *30*, 976–992. [CrossRef]
104. Ábalos, B. Omphacite fabric variation in the Cabo Ortegal eclogite (NW Spain): Relationships with strain symmetry during high-pressure deformation. *J. Struct. Geol.* **1997**, *19*, 621–637. [CrossRef]
105. Boudier, F.; Baronnet, A.; Mainprice, D. Serpentine mineral replacements of natural olivine and their seismic implications: Oceanic lizardite versus subduction-related antigorite. *J. Petrol.* **2010**, *51*, 495–512. [CrossRef]
106. Cao, S.; Liu, J.; Leiss, B. Orientation-related deformation mechanisms of naturally deformed amphibole in amphibolite mylonites from the Diancang Shan, SW Yunnan, China. *J. Struct. Geol.* **2010**, *32*, 606–622. [CrossRef]
107. Cao, Y.; Jung, H.; Ma, J. Seismic Properties of a Unique Olivine-Rich Eclogite in the Western Gneiss Region, Norway. *Minerals* **2020**, *10*, 774. [CrossRef]